

# Probe the regolith characteristics of asteroids from 9-years infrared observations of WISE/NEOWISE: A case study of the Main-Belt Object (656) Beagle

LIANG-LIANG YU<sup>1</sup>

<sup>1</sup>*Institute of Science and Technology for Deep Space Exploration, Nanjing University-Suzhou Campus, Suzhou, 215163, China*

(Received MM DD, YY; Revised MM DD, YY; Accepted MM DD, YY)

## ABSTRACT

This work presents data processing, fitting procedure, modelling and analyzing of 9-years infrared light curves provided by the WISE/NEOWISE telescope, by which the regolith characteristics of Main-Belt Object (656) Beagle is studied. We determine Beagle's effective diameter  $D_{\text{eff}} = 57.3_{-2.2}^{+4.5}$  km, geometric albedo  $p_v = 0.05_{-0.007}^{+0.004}$ , mean roughness  $\theta_{\text{RMS}} = 44 \pm 4^\circ$ , mean grain size  $b = 100_{-90}^{+350}$   $\mu\text{m}$ , mean specific heat capacity  $c_p = 173 \sim 516$   $\text{JKg}^{-1}\text{K}^{-1}$ , mean thermal conductivity  $\kappa = 0.7 \sim 1.3 \times 10^{-3}$   $\text{Wm}^{-1}\text{K}^{-1}$  and mean thermal inertia  $\Gamma = 14 \sim 32$   $\text{Jm}^{-2}\text{s}^{-0.5}\text{K}^{-1}$ . The albedo of Beagle is a little anomalous that the albedos of Beagle's neighbouring asteroids are more close to Themis, rather than Beagle itself. The W1-band near-infrared light curves don't reveal significant heterogeneous NIR features on the surface of Beagle, being inconsistent with the expectation of a family parent that has members with diverse NIR spectral types. These results add new clues of Beagle probably being an interloper or a sister, rather than the parent of its neighbouring asteroids including the first main-belt comet (MBC) 133P, hence may lead to new scenarios about the origin of famous MBC 133P. Besides, we found that asteroidal shape models from inversion of optical light curves are imperfect for modeling infrared lightcurves, thus could mislead evaluations of both the heterogeneity of regolith reflectivity at near infrared and thermophysical characteristics at thermal infrared.

*Keywords:* Light curves — Infrared photometry — Small Solar System bodies — Main belt asteroids — Asteroid surfaces

## 1. INTRODUCTION

The main-belt asteroid (656) Beagle (hereafter Beagle for short) came into the sight of astronomers since it was proposed to be the parent of the famous main-belt comet (MBC) 133P/Elst-Pizarro (Nesvorný et al. 2008). And the Beagle family is proposed to be a young family with an age of  $< 10$  Myr (Nesvorný et al. 2008) or  $\sim 14$  Myr (Carruba 2019). Then the story about the origin of 133P is widely accepted as the following scenario: 133P is a young icy fragment of Beagle, which is a daughter of the icy main-belt object (24) Themis, on which absorption feature of water ice was observed by the IRTF spectra (Campins et al. 2010; Rivkin & Emery 2010). The formation scenario was somewhat supported by the work of (Fornasier et al. 2016), which reported Beagle to have a geometric albedo of  $p_v = 0.0782 \pm 0.0222$ , being similar to the geometric albedos of its neighbouring asteroids (mean  $p_v = 0.0941 \pm 0.0055$ ) and potential parent (24) Themis ( $p_v = 0.0641 \pm 0.0157$ ).

Besides, Fornasier et al. (2016) also found that the neighbouring asteroids of Beagle exhibit diverse spectral types based on the reflectance spectrum at near infrared (NIR), implying that the composition of these asteroids differs from each other. If these neighbouring asteroids of Beagle were formed from the same impact event, then their diverse compositions may originate from the parent, or from the impactor, or produced by the high temperature and pressure during impact process. According to Michel et al. (2015), if a parent body is heterogeneous in composition, then the resulting family is expected to show a variety of spectral properties within its members. On the other hand, although the original parent may not have spectral variability on its surface, the impact that produced heterogeneous members will make the survived parent to show surface heterogeneity. For example, Vesta is observed to show heterogeneous surface features due to impact exposing heterogeneous subsurface and upper crust materials (Rousseau, De Sanctis & Raponi et al 2021). Therefore, if Beagle is the survived parent of these neighbouring asteroids with diverse compositions, then Beagle is expected to contain diverse compositions on its surface and show heterogeneous NIR features across its surface.

However, [Mainzer et al. \(2016\)](#) reported Beagle to have a very low geometric albedo  $p_v = 0.045 \pm 0.005$ , being even lower than that of (24) Themis. On the other hand, the recent work of [Yu et al. \(2020\)](#) found that 133P is more likely to have an old age  $> 100$  Myr, being inconsistent with the young age  $< 10$  Myr of the Beagle family. These new observations and theoretical predictions thus raise the question of whether Beagle having genetic connections with 133P and (24) Themis.

So in this work, we attempt to use more data and new method to investigate whether asteroid Beagle has a geometric albedo as low as  $\sim 0.05$  and significant heterogeneous reflectivity at near infrared. This objective can be achieved by analyzing the multi-year infrared light curves of Beagle from WISE/NEOWISE with the well-tested thermophysical model — RSTPM ([Yu & Ip 2021](#)). As the WISE/NEOWISE observations of main-belt objects at band-W1 are dominated by sunlight reflection at near infrared. In addition, heterogeneity of regolith thermophysical characteristics can also be evaluated from the other three bands of W2, W3, and W4.

## 2. THE RADIOMETRIC MODEL

### 2.1. Observations and data processing

The *Wide-field Infrared Survey Explorer* (WISE) mission has mapped entire sky in four bands around 3.4 (W1), 4.6 (W2), 12 (W3), and 22 (W4)  $\mu\text{m}$  with resolutions from 6.1'' to 12'' ([Wright et al. 2010](#)). All four bands were imaged simultaneously, and the exposure times were 7.7 s in W1 and W2, and 8.8 s in W3 and W4 ([Wright et al. 2010](#)). The four-bands survey started from 2010 January 7, and ended on 2010 August 6 after the outer cryogen tank was exhausted, making the W4 channel be no longer able to be used to obtain survey data. The W3 channel continued operation until 2010 September 29 when the inner cryogen reserve was exhausted, while the W1 and W2 channel kept working until the telescope was set into hibernation on 2011 February 1 ([Mainzer et al. 2011](#); [Cutri et al. 2012](#)). The two-band survey was then resumed on 2013 December 13 (known as NEOWISE) ([Mainzer et al. 2014](#); [Cutri et al. 2015](#)), and is still in service, which has obtained nearly 10-year observations.

We found 9-years observations of Beagle from the WISE archive (see the website of the NASA/IPAC Infrared Science Archive <http://irsa.ipac.caltech.edu/>). The datasets are summarized in Table 1.

#### 2.1.1. Flux colour corrections

All the four-band data need colour corrections, especially for the W1 and W2-band data, the infrared fluxes of which contain not only self-thermal emission but also sunlight diffused from the object's surface, thus the color corrections should be done separately for the thermal component and the reflection component, as the color correction factors are different. Besides, the color correction factor for the thermal component is temperature dependent, thus will have different value if the helio-centric distance was different for each observation epoch. So we implement the color-correction procedure as follows:

**Table 1.** The collected WISE/NEOWISE observations of (656) Beagle from 2010 to 2019.

UTC	Bands	Obs Num	$r_{\text{helio}}$ (AU)	$\Delta_{\text{obs}}$ (AU)	$\alpha$ ( $^\circ$ )
Jan. 31-01, 2010	W1-4	14	2.82	2.66	20.42
Jul. 26-28, 2010	W1-4	16	3.03	2.78	-19.51
Feb. 15-16, 2014	W1-2	11	3.01	2.81	-19.17
Dem. 05-06, 2014	W1-2	14	2.73	2.52	21.11
May. 19-20, 2015	W1-2	16	2.75	2.40	-21.28
Mar. 09-11, 2016	W1-2	11	3.06	2.88	18.95
Aug. 20-21, 2016	W1-2	11	3.27	2.88	-17.52
May. 14-15, 2017	W1-2	14	3.52	3.39	16.70
Oct. 19-20, 2017	W1-2	12	3.57	3.12	-15.32
Jul. 17-18, 2018	W1-2	11	3.49	3.33	16.95
Dem. 12-13, 2018	W1-2	13	3.35	2.84	-15.66
Oct. 03-04, 2019	W1-2	12	2.99	2.81	19.58

$r_{\text{helio}}$ : heliocentric distance;

$\Delta_{\text{obs}}$ : observation distance;

$\alpha$ : solar phase angle.

First, convert the data-base magnitude to flux without any color correction, giving the total integrated flux  $F(\lambda \pm \Delta\lambda)_{\text{tot,obs}}$  for each band. The derived band-integrated fluxes together with the observation geometry are listed in Table 2 and 3, and each flux should at least have an associated uncertainty of  $\pm 10$  percent according to [Wright et al. \(2010\)](#);

Second,  $F(\lambda \pm \Delta\lambda)_{\text{tot,obs}}$  contains both integrated thermal emission and sunlight reflection, and can be modelled as

$$F(\lambda \pm \Delta\lambda)_{\text{tot,model}} = F(\lambda)_{\text{rl}} * f_{c,\text{rl}} + F(\lambda)_{\text{th}} * f_{c,\text{th}}, \quad (1)$$

where  $F(\lambda)_{\text{rl}}$  and  $F(\lambda)_{\text{th}}$  represent the monochromatic sunlight reflection and thermal emission that can be calculated from reflection and thermal models;  $f_{c,\text{rl}}$  and  $f_{c,\text{th}}$  stand for the color correction factor of the reflection component and the thermal component respectively; here  $f_{c,\text{rl}}$  can be chosen to be the color correction factor of G2V star, thus fixing

$$f_{c,\text{rl}} = 1.0049, 1.0193, 1.0024, 1.0012$$

for the four band — W1, W2, W3 and W4 respectively ([Wright et al. 2010](#));

Third, since  $f_{c,\text{th}}$  is temperature dependent, so its value for each band will be obtained from an interpolation procedure according to the effective temperature

$$T_{\text{eff}} = \left[ \frac{(1 - A_B)L_\odot}{\varepsilon\sigma\pi d_\odot^2} \right]^{1/4} \approx \frac{300 \text{ K}}{\sqrt{d_\odot}}, \quad (2)$$

of the asteroid at the time of observation, on the basis of the Table 1 of [Wright et al. \(2010\)](#). In Equation (2),  $d_\odot$  means the

**Table 2.** WISE observations of (656) Beagle. The derived fluxes are band-integrated fluxes of each band without color correction. Each flux should have an associated uncertainty of  $\pm 10$  percent according to Wright et al. (2010).

MJD	W1 (mJy)	W2 (mJy)	W3 (Jy)	W4 (Jy)	$r_{\text{helio}}$ (AU)	$\Delta_{\text{obs}}$ (AU)	$\alpha$ ( $^{\circ}$ )
55227.504	1.49	6.64	1.26	3.18	2.82	2.67	20.42
55227.637	1.44	6.71	1.16	2.99	2.82	2.67	20.42
55227.637	1.51	6.57	1.22	3.22	2.82	2.67	20.42
55227.769	1.42	5.44	0.94	2.58	2.82	2.67	20.42
55227.901	0.96	-	0.74	2.16	2.82	2.66	20.42
55228.034	0.77	2.95	0.54	1.64	2.82	2.66	20.42
55228.100	1.53	6.93	1.16	3.37	2.82	2.66	20.42
55228.166	0.73	2.84	0.57	1.69	2.82	2.66	20.42
55228.232	1.58	7.36	1.23	3.34	2.82	2.66	20.42
55228.298	0.87	4.14	0.75	2.25	2.82	2.66	20.42
55228.364	1.29	5.95	1.06	2.93	2.82	2.66	20.42
55228.497	1.17	4.68	0.87	2.44	2.82	2.66	20.42
55228.629	0.95	3.90	0.73	1.95	2.82	2.65	20.42
55228.762	-	3.23	0.55	1.59	2.82	2.65	20.42
55403.908	1.17	3.00	0.68	2.18	3.03	2.77	-19.50
55404.040	0.80	-	0.50	1.70	3.03	2.77	-19.50
55404.172	0.58	1.73	0.40	1.34	3.03	2.77	-19.51
55404.173	0.58	1.68	0.41	1.34	3.03	2.77	-19.51
55404.305	0.62	1.59	0.36	1.19	3.03	2.77	-19.51
55404.371	1.21	3.68	0.88	2.54	3.03	2.78	-19.51
55404.437	0.76	2.05	0.41	1.30	3.03	2.78	-19.51
55404.503	1.01	2.70	0.70	2.32	3.03	2.78	-19.51
55404.569	0.90	2.67	0.58	1.76	3.03	2.78	-19.51
55404.636	0.98	2.33	0.63	2.01	3.03	2.78	-19.51
55404.768	0.81	2.02	0.48	1.63	3.03	2.78	-19.51
55404.900	0.38	-	0.35	1.20	3.03	2.78	-19.51
55405.032	0.50	1.43	0.33	1.02	3.03	2.79	-19.52
55405.032	0.53	1.26	0.33	1.04	3.03	2.79	-19.52
55405.165	0.68	2.09	0.45	1.41	3.03	2.79	-19.52
55405.165	0.65	2.31	0.50	1.53	3.03	2.79	-19.52

heliocentric distance in AU;  $L_{\odot}$  is the Solar constant, about  $1361.5 \text{ Wm}^{-2}$ ,  $A_B$  is the surface bond albedo;  $\varepsilon$  is the averaged thermal emissivity over the entire emission spectrum of the surface and  $\sigma$  is the Stefan Boltzmann constant;

Finally, calculate the theoretical monochromatic sunlight reflection  $F(\lambda)_{\text{rl}}$  and thermal emission  $F(\lambda)_{\text{th}}$  via our RSTPM code, and then obtain the theoretical total flux  $F(\lambda \pm \Delta\lambda)_{\text{tot,model}}$  via Equation (1), so as to do comparison with the observed total flux  $F(\lambda \pm \Delta\lambda)_{\text{tot,obs}}$  at the first step.

### 2.1.2. Anomalous data removal

Due to some noise pollution, e.g. cosmic rays and zodiacal light, some of the observed fluxes may deviate too much from the actual emission of the target. Such anomalous data need to be removed from the parameter inversion procedure, so as to make the results about the physical characteristics of the target get to be more close to reality.

The basic way to remove anomalous data is on the basis of 'signal to noise ratio ( $snr$ )'. For the WISE/NEOWISE observations of asteroids, generally we remove the data with  $snr < 3$ .

For asteroids with shape model, there is also an additional way to remove anomalous data. As the multi-year data of

WISE and NEOWISE make it possible to generate infrared light curves, so by doing comparisons between the observational and theoretical infrared light curves, the data sets deviate too much from the theoretical curves can be treated as anomalous data and remove them can make the reversion procedure get better results.

## 2.2. Themophysical model

As has been mentioned above, this work uses the thermo-physical model for realistic surface layers on airless small bodies — RSTPM (Yu & Ip 2021). The model considers not only real shape and rough surface, but also real orbital cycle, rotational cycle, and even temperature dependent thermal parameters in the simulation process, as well as contribution of sunlight reflection in the infrared radiometric procedure.

In comparison to previous models, the advantages of the RSTPM are: (1) A different mathematical technique is used to solve the influence of surface roughness on the energy balance equation of surface boundary; (2) For the aim to remove the degeneracy of thermal inertia and roughness by interpreting multi-epoch thermal light-curves, variation of thermal parameters due to temperature variation caused by orbital cycle and rotation cycle is taken into consideration; (3) A combination model of simultaneously computing thermal emission and sunlight-reflection under the same surface topography is proposed to fit infrared data in case of the data containing significant sunlight reflection.

So RSTPM has advantages for the small bodies which has regolith on the surface and has large orbital eccentricity or an obliquity close to 90 degrees. And for the target asteroid Beagle, we assume it have fine regolith on its surface, as it has a much larger size than Eros, Ryugu and Bennu.

## 3. FITTING PROCEDURE AND RESULTS

### 3.1. The Input and Free Parameters

In order to interpret the multi-year observations, RSTPM needs several input parameters, including observation geometry, shape model, spin orientation, rotation phase  $ph$ , scattering weight-factor  $w_f$ , geometric albedo  $p_v$ , effective diameter  $D_{\text{eff}}$ , mean grain radius  $b$ , and roughness fraction  $f_r$ , which can be related to the root-mean-square slope as  $\theta_{\text{RMS}} = \sqrt{f_r} \times 50^{\circ}$  (Yu & Ip 2021).

The observation geometry at the time of each observation can be easily obtained according to the orbit of Beagle and WISE. The spin period and spin orientation together with shape model of Beagle are also known by light curve inversion method from the DAMIT database. The utilized shape model of Beagle is shown in Figure 1, where  $ph$  represents rotational phase defined as  $ph = 1 - \varphi/(2\pi)$ , in which  $\varphi$  is the local longitude of the observer in the body-fixed coordinate system.

The scattering weight-factor  $w_f$  is introduced in the combined Lambert-Lommel-Seeliger law via

$$C_L(\psi_i, \psi_{o,i}, \alpha, w_f) = f(\alpha) \left( w_f + \frac{1}{\psi_i + \psi_{o,i}} \right), \quad (3)$$

**Table 3.** NEOWISE observations of (656) Beagle. The derived fluxes are band-integrated fluxes of each band without color correction. Each flux should have an associated uncertainty of  $\pm 10$  percent according to [Wright et al. \(2010\)](#).

MJD	W1 (mJy)	W2 (mJy)	$r_{\text{helio}}$ (AU)	$\Delta_{\text{obs}}$ (AU)	$\alpha$ ( $^{\circ}$ )	MJD	W1 (mJy)	W2 (mJy)	$r_{\text{helio}}$ (AU)	$\Delta_{\text{obs}}$ (AU)	$\alpha$ ( $^{\circ}$ )
56703.138	0.99	2.23	3.01	2.80	-19.16	57887.678	0.32	0.61	3.52	3.40	16.70
56703.270	0.75	1.69	3.01	2.80	-19.16	57887.809	0.25	-	3.52	3.40	16.70
56703.401	0.54	1.21	3.01	2.80	-19.16	57887.940	0.36	0.65	3.52	3.39	16.70
56703.533	0.66	1.68	3.01	2.81	-19.17	57887.940	0.41	0.52	3.52	3.39	16.70
56703.599	1.18	3.22	3.01	2.81	-19.17	57888.071	0.54	0.80	3.52	3.39	16.70
56703.665	1.01	2.80	3.01	2.81	-19.17	57888.136	0.47	0.67	3.52	3.39	16.70
56703.731	1.14	2.62	3.01	2.81	-19.17	57888.202	0.64	0.86	3.52	3.39	16.70
56703.797	1.05	3.13	3.01	2.81	-19.17	57888.267	0.34	0.47	3.52	3.39	16.70
56703.994	0.60	1.36	3.01	2.81	-19.18	57888.333	0.68	1.23	3.52	3.39	16.71
56704.126	0.70	1.54	3.01	2.81	-19.18	57888.333	0.71	1.38	3.52	3.39	16.71
56704.258	0.72	2.64	3.01	2.82	-19.18	57888.398	0.28	0.51	3.52	3.39	16.71
56996.277	1.71	8.14	2.73	2.53	21.12	57888.529	0.36	0.45	3.52	3.39	16.71
56996.409	1.51	7.25	2.73	2.53	21.12	57888.660	0.56	0.82	3.52	3.38	16.71
56996.540	1.17	5.58	2.73	2.53	21.11	57888.791	0.60	0.98	3.52	3.38	16.71
56996.672	0.84	3.77	2.73	2.52	21.11	58045.491	0.40	0.53	3.57	3.12	-15.28
56996.737	1.91	9.87	2.73	2.52	21.11	58045.622	0.38	0.46	3.57	3.12	-15.29
56996.803	0.66	3.16	2.73	2.52	21.11	58045.622	0.31	0.53	3.57	3.12	-15.29
56996.869	1.84	9.27	2.73	2.52	21.11	58045.753	0.44	0.59	3.57	3.12	-15.30
56996.934	0.94	4.62	2.73	2.52	21.11	58045.884	0.56	0.97	3.57	3.12	-15.31
56997.000	1.64	8.15	2.73	2.52	21.11	58046.015	0.57	1.06	3.57	3.12	-15.32
56997.066	1.53	7.41	2.73	2.52	21.11	58046.080	0.50	0.69	3.57	3.13	-15.32
56997.132	1.37	6.12	2.73	2.52	21.11	58046.146	0.93	1.08	3.57	3.13	-15.33
56997.263	0.93	4.10	2.73	2.52	21.11	58046.211	0.39	0.42	3.57	3.13	-15.34
56997.394	0.76	3.28	2.73	2.51	21.11	58046.342	0.39	0.54	3.57	3.13	-15.35
56997.526	0.96	4.15	2.73	2.51	21.10	58046.473	0.52	0.57	3.57	3.13	-15.36
57161.421	1.82	7.32	2.75	2.39	-21.25	58046.604	0.67	0.94	3.57	3.13	-15.37
57161.552	1.41	5.31	2.75	2.40	-21.26	58316.418	0.33	0.60	3.49	3.34	16.95
57161.552	1.65	5.52	2.75	2.40	-21.26	58316.549	0.44	0.84	3.49	3.34	16.95
57161.683	1.20	3.57	2.75	2.40	-21.26	58316.680	0.57	0.95	3.49	3.34	16.95
57161.814	0.87	2.76	2.75	2.40	-21.27	58316.811	0.67	1.26	3.49	3.33	16.95
57161.880	1.87	7.80	2.75	2.40	-21.27	58316.942	0.62	1.20	3.49	3.33	16.95
57161.946	0.89	3.42	2.75	2.40	-21.28	58317.007	0.36	0.53	3.49	3.33	16.95
57161.946	0.87	3.51	2.75	2.40	-21.28	58317.073	0.63	1.03	3.49	3.33	16.95
57162.011	1.98	8.11	2.75	2.40	-21.28	58317.138	0.37	0.71	3.49	3.33	16.95
57162.077	1.22	5.61	2.75	2.40	-21.28	58317.269	0.59	0.85	3.49	3.33	16.95
57162.143	1.63	5.65	2.75	2.40	-21.29	58317.400	0.72	1.18	3.49	3.32	16.95
57162.274	1.19	4.16	2.75	2.41	-21.29	58317.531	0.57	0.97	3.49	3.32	16.95
57162.405	0.95	3.04	2.75	2.41	-21.30	58464.862	0.47	0.90	3.35	2.83	-15.60
57162.536	1.02	3.38	2.75	2.41	-21.31	58464.992	0.62	1.29	3.35	2.84	-15.62
57162.536	0.89	3.22	2.75	2.41	-21.31	58464.992	0.71	1.27	3.35	2.84	-15.62
57162.667	1.04	5.02	2.75	2.41	-21.31	58465.123	0.86	1.63	3.35	2.84	-15.63
57456.914	1.39	3.76	3.06	2.89	18.95	58465.254	1.03	1.87	3.35	2.84	-15.65
57457.045	1.02	3.40	3.06	2.89	18.95	58465.320	0.55	0.77	3.35	2.84	-15.66
57457.176	1.19	3.26	3.06	2.89	18.95	58465.385	1.13	2.01	3.35	2.84	-15.66
57457.307	0.98	2.63	3.06	2.89	18.95	58465.450	0.40	-	3.35	2.84	-15.67
57457.373	1.24	2.93	3.06	2.89	18.95	58465.451	0.42	0.78	3.35	2.84	-15.67
57457.438	0.93	2.10	3.06	2.88	18.95	58465.516	0.97	1.61	3.35	2.84	-15.68
57457.635	-	3.98	3.06	2.88	18.94	58465.581	0.67	1.19	3.35	2.84	-15.69
57457.766	1.18	3.48	3.06	2.88	18.94	58465.712	0.84	1.45	3.35	2.84	-15.70
57457.897	1.08	2.94	3.06	2.88	18.94	58465.843	0.98	1.83	3.35	2.85	-15.72
57458.028	0.68	2.09	3.06	2.88	18.94	58759.742	0.50	1.67	2.99	2.82	19.58
57458.159	0.68	1.62	3.06	2.88	18.94	58759.742	0.55	1.67	2.99	2.82	19.58
57620.359	0.44	-	3.27	2.88	-17.49	58759.872	0.59	2.11	2.99	2.82	19.58
57620.490	0.48	0.99	3.27	2.88	-17.50	58760.134	0.92	3.20	2.99	2.81	19.58
57620.621	0.81	1.47	3.27	2.88	-17.51	58760.200	0.70	2.54	2.99	2.81	19.58
57620.752	0.92	2.06	3.27	2.88	-17.52	58760.265	1.06	4.34	2.99	2.81	19.58
57620.817	0.56	1.06	3.27	2.88	-17.52	58760.330	0.76	2.04	2.99	2.81	19.58
57620.883	-	2.43	3.27	2.88	-17.52	58760.396	1.21	4.10	2.99	2.81	19.58
57620.948	0.58	0.92	3.27	2.88	-17.53	58760.461	0.66	1.62	2.99	2.81	19.58
57621.014	0.84	2.00	3.27	2.89	-17.53	58760.592	0.68	2.35	2.99	2.81	19.58
57621.079	0.49	1.03	3.27	2.89	-17.53	58760.723	0.90	3.02	2.99	2.80	19.58
57621.210	0.71	1.56	3.27	2.89	-17.54	58760.854	1.23	4.36	2.98	2.80	19.58
57621.341	0.76	1.93	3.27	2.89	-17.55						

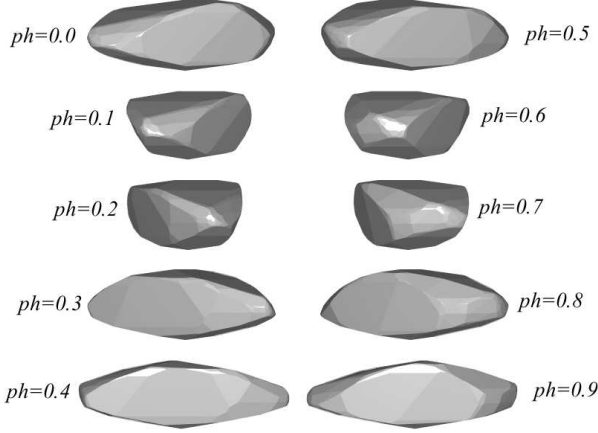


**Figure 1.** The light-curve inversion shape model of (656) Beagle from the DAMIT database.  $ph$  represents rotational phase defined as  $ph = 1 - \varphi/(2\pi)$ , in which  $\varphi$  is the local longitude of the observer in the body-fixed coordinate system.

where  $C_L$  represents a correction coefficient to the Lambertian reflection,  $\psi_i$  and  $\psi_{o,i}$  are the cosines of the incident angle and emergence angle on facet  $i$  respectively,  $\alpha$  is the solar phase angle;  $f(\alpha)$  is the phase correction function, according to (Kaasalainen, Torppa & Muinonen 2001),

$$f(\alpha) \sim 0.5 \exp(-\alpha/0.1) - 0.5\alpha + 1.$$

Parameter  $w_f$  represents the weight of Lambertian term in the scattering law, and is an artificial factor to interpret sunlight refraction. Its physical significance isn't that clear, thus we only need a scattering weight-factor  $w_f$  that could achieve best-fitting degree to the observations.

The effective diameter  $D_{\text{eff}}$ , defined by the diameter of a sphere with the same area to that of the shape model, can be related to the geometric albedo  $p_v$  and absolute visual magnitude  $H_v$  via:

$$D_{\text{eff}} = \frac{1329 \times 10^{-H_v/5}}{\sqrt{p_v}} \text{ (km)}. \quad (4)$$

In addition, the geometric albedo  $p_v$  is related to the effective Bond albedo  $A_{\text{eff,B}}$  by

$$A_{\text{eff,B}} = p_v(0.290 + 0.684G), \quad (5)$$

in which  $G$  is the slope parameter in the  $H, G$  magnitude system of Bowell et al. (1989). As for Beagle, this work uses  $H_v = 10.8$  and  $G = 0.15$  (IAU MPC).

So parameters including geometric albedo  $p_v$ , roughness  $\theta_{\text{RMS}}$ , and mean grain radius  $b$ , are the free parameters that would be evaluated from the fitting procedures.

### 3.2. Wavelength-dependent Thermal Emissivity

In general cases, an constant thermal emissivity  $\epsilon \approx 0.9$  is assumed for each band in the model to calculate the thermal

**Table 4.** Fixed input parameters of (656) Beagle.

Properties	Value
Facets of shape model	1144
Nodes of shape model	574
Spin ecliptic orientation	(237°, 86°)
Spin period	7.0331 hr
Absolute visual magnitude $H_v$	10.8
Slope parameter $G$	0.15
Mean thermal emissivity $\epsilon$	0.9
Regolith grain density $\rho_g$	3110 kgm <sup>-3</sup>
Regolith porosity $\phi$	0.5

emission component. However, in the case of Beagle, we find that, if using wavelength-dependent thermal emissivity, the model results match the observations better, as shown in Figure 2.

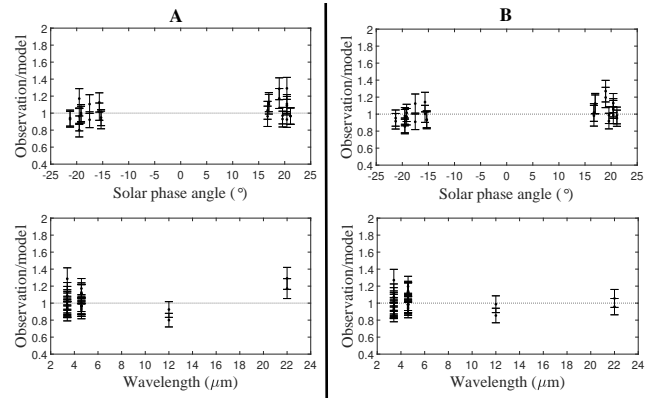


**Figure 2.** The observation/model ratios as a function of wavelength (upper panel) and solar phase angle (under panel) for the case of best-fit parameters. Panel A (left): best-fit model results are obtained by using constant input thermal emissivity  $\epsilon \approx 0.9$ ; Panel B (right): using wavelength-dependent thermal emissivity  $\epsilon \approx 0.72, 0.72, 0.72, 0.95$  for the W1, W2, W3, W4 band respectively.

After a process of adjusting the thermal emissivity to fit the observations, we find that, the fitting degree can be the best by using  $\epsilon \approx 0.72, 0.72, 0.72, 0.95$  for the W1, W2, W3, W4 band respectively. The thermal emissivity of band W4 is almost close to 1, indicating that band W4 is near the Wien peak of the thermal emission spectra of Beagle.

On the other hand, with RSTPM, the fraction of sunlight-reflection in the observed flux of Beagle for each band of WISE/NEOWISE can be evaluated, the results are plotted in Figure 3. The W1-band is reflection dominated with reflection ratio  $\sim 95\%$ , the W2-band becomes thermal emission dominated but have significant reflection ratio between  $10 \sim 45\%$ , finally the W3 and W4 are almost all thermal emission with reflection ratio  $< 0.1\%$ .

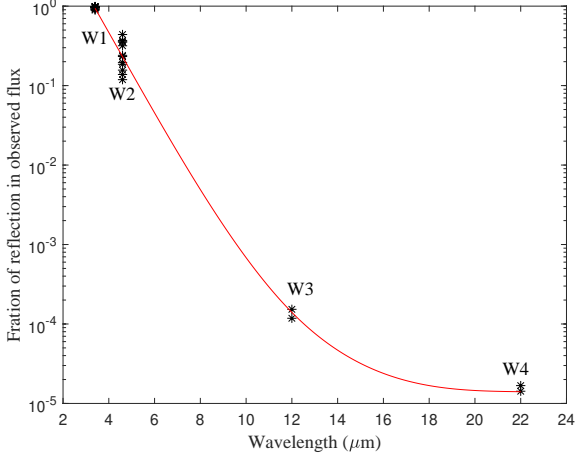


**Figure 3.** The fraction of sunlight-reflection in the observed flux of Beagle for each band of WISE/NEOWISE.

### 3.3. Results of Roughness, Grain Size and Albedo

By adopting different thermal emissivity for the four band, we then fit the observations by scanning roughness  $\theta_{\text{RMS}}$  in the range of  $0 \sim 50^\circ$  and mean grain radius  $b$  in the range of  $1 \sim 1000 \mu\text{m}$ . With each pair of  $(\theta_{\text{RMS}}, b)$ , a best-fit geometric albedo  $p_v$  together with effective diameter  $D_{\text{eff}}$  is found to compute the reduced  $\chi_r^2$ . The results are presented in Figure 4 as a contour of  $\chi_r^2(\theta_{\text{RMS}}, b)$ .

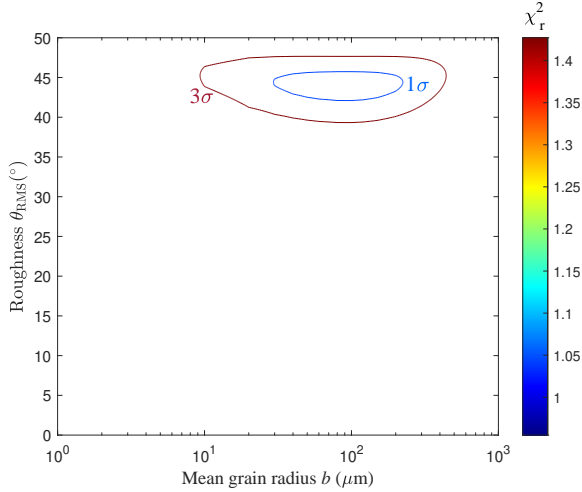


**Figure 4.** The contour of  $\chi_r^2(\theta_{\text{RMS}}, b)$ , which is obtained by fitting the observations with two free parameters: the roughness RMS slope  $\theta_{\text{RMS}}$  and the mean grain radius  $b$ . The blue region stands for the  $1\sigma$ -level constraint, and the red region represents the  $3\sigma$ -level constraint.

According to Figure 4, a well constrained  $1\sigma$ -level limit is derived for roughness  $\theta_{\text{RMS}}$  and mean grain radius  $b$ , giving  $\theta_{\text{RMS}} = 44 \pm 2^\circ$ ,  $b = 100_{-70}^{+130} \mu\text{m}$  respectively.  $3\sigma$ -level constraint for roughness is derived as  $\theta_{\text{RMS}} = 44 \pm 4^\circ$ , whereas

for mean grain radius, a relatively wide  $3\sigma$ -level limit is obtained as  $b = 100_{-90}^{+350} (10 \sim 450) \mu\text{m}$ .

According to the above derived  $1\sigma$  and  $3\sigma$  ranges of roughness and mean grain radius, the corresponding geometric albedo  $p_v$  and  $\chi_r^2$  are picked out, leading to the  $p_v \sim \chi_r^2$  relation as shown in Figure 5. In this way, we obtain the  $1\sigma$  and  $3\sigma$ -level limits of geometric albedo as  $p_v = 0.05_{-0.003}^{+0.002}$  and  $p_v = 0.05_{-0.007}^{+0.004}$  respectively, and simultaneously the effective diameter of Beagle is obtained as  $D_{\text{eff}} = 57.3_{-1.1}^{+1.8} \text{ km}$  ( $1\sigma$ ) and  $D_{\text{eff}} = 57.3_{-2.2}^{+4.5} \text{ km}$  ( $3\sigma$ ).

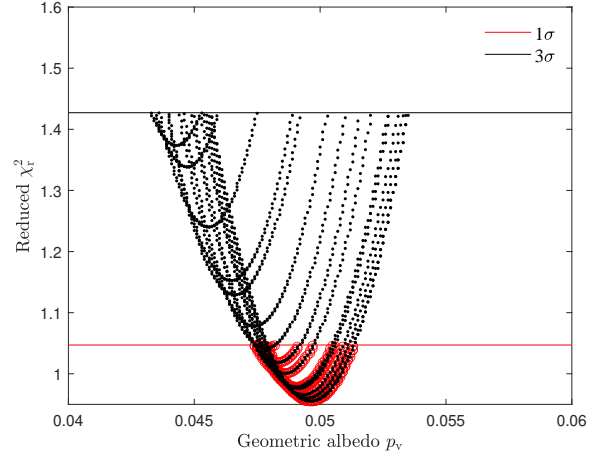


**Figure 5.**  $p_v \sim \chi_r^2$  profiles fit to the observations in consideration of the derived  $1\sigma$  and  $3\sigma$  ranges of roughness and mean grain radius.

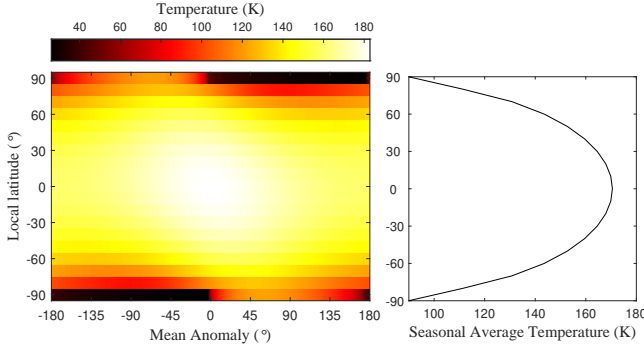
### 3.4. Regolith thermophysical characteristics

Thermal inertia is a strong function of temperature. Now with the above derived profile of mean grain radius, we can evaluate the change of surface thermal inertia of Beagle due to the influence of seasonal temperature variation according to the relationships between thermal inertia, thermal conductivity, specific heat capacity and temperature given in Yu & Ip (2021).

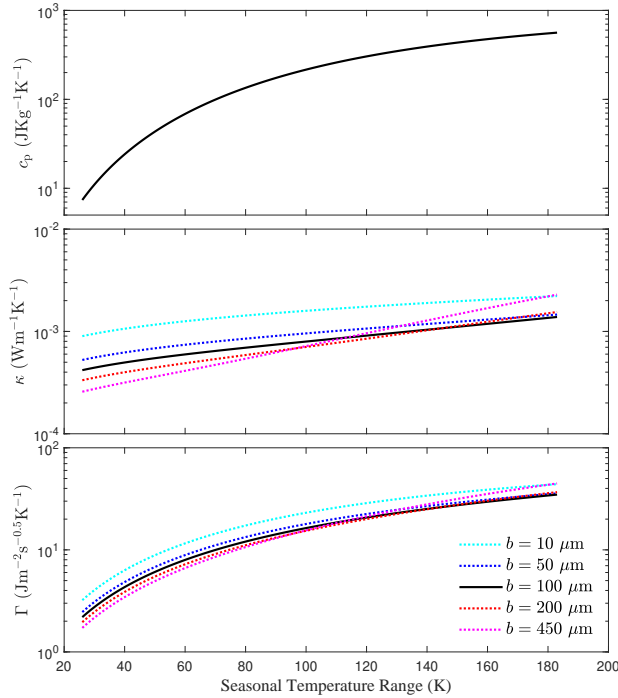
In the left panel of Figure 6, a map of surface temperature of Beagle is plotted as a function of local latitude and orbital mean anomaly. Each temperature has been averaged over one rotational period. We can clearly see that temperature on each local latitude can reach maximum (summer) or minimum (winter) at different orbital positions as a result of seasonal effect. Temperature on the poles can vary from  $\sim 26 \text{ K}$  to  $\sim 183 \text{ K}$ .

Figure 7 shows that, if considering seasonal temperature variation and  $3\sigma$ -level range of mean grain radius  $b$ , the regolith thermal inertia, thermal conductivity, specific heat capacity of Beagle can be estimated to vary between  $2 \sim 45 \text{ Jm}^{-2}\text{s}^{-0.5}\text{K}^{-1}$ ,  $0.3 \sim 2.3 \times 10^{-3} \text{ Wm}^{-1}\text{K}^{-1}$ ,  $7 \sim 562 \text{ JKg}^{-1}\text{K}^{-1}$ .

Despite the fact that thermal parameters is temperature dependent, the majority of relevant works ignore such temperature dependence and only estimate the average values. For



**Figure 6.** Left panel: Seasonal variation of the diurnal-averaged surface temperature as a function of local latitude. Right panel: Seasonal average temperature of each local latitude. The so-called local latitude is defined as the complementary angle of the angle between the local normal vector and the rotation axis.



**Figure 7.** The regolith specific heat capacity  $c_p$ , thermal conductivity  $\kappa$ , and thermal inertia  $\Gamma$  of Beagle in consideration of seasonal temperature variation and  $3\sigma$ -level range of mean grain radius  $b$ .  $\Gamma = \sqrt{(1 - \phi)\rho_g c_p \kappa}$ , and porosity  $\phi \sim 0.5$ , regolith grain density  $\rho_g = 3110 \text{ kgm}^{-3}$ .

comparison with such existing results, we estimate the seasonal average thermal parameters of Beagle with inputs of the derived mean grain radius and seasonal averaged temperature. The seasonal average temperature would be a function of local latitude,  $\bar{T}(\theta)$ , and can be estimated as

$$(1 - A_{\text{eff,B}})\bar{L}_s(\theta) = \varepsilon\sigma\bar{T}(\theta)^4, \quad (6)$$

where  $A_{\text{eff,B}}$  is the bond albedo,  $\varepsilon \sim 0.9$  is the average thermal emissivity,  $\bar{L}_s(\theta)$  is the annual average incoming solar flux on each latitude. The results are presented in The right panel of Figure 6, giving the seasonal average temperature of Beagle to be  $90 \sim 170 \text{ K}$ , and accordingly the average specific heat capacity

$$c_p = 173 \sim 516 \text{ JKg}^{-1}\text{K}^{-1},$$

the average thermal conductivity

$$\kappa = 0.7 \sim 1.3 \times 10^{-3} \text{ Wm}^{-1}\text{K}^{-1},$$

and the average thermal inertia

$$\Gamma = \sqrt{(1 - \phi)\rho_g c_p \kappa} = 14 \sim 32 \text{ Jm}^{-2}\text{s}^{-0.5}\text{K}^{-1},$$

where the porosity  $\phi$  uses 0.5, and the regolith grain density  $\rho_g$  uses  $3110 \text{ kgm}^{-3}$  (Opeil et al. 2010).

### 3.5. Infrared light curves

With the above derived physical and thermophysical parameters of Beagle, now we are able to determine the rotation phase of Beagle at each time of WISE/NEOWISE observation by doing comparisons between the observational and theoretical light curves. To do so, the 3D shape model is used to define the local body-fixed coordinate system, where the z-axis is chosen to be the rotation axis. Moreover, if we define the view angle of one observation with respect to the body-fixed coordinate system to be  $(\varphi, \theta)$ , where  $\varphi$  stands for local longitude, and  $\theta$  means local latitude, then the rotational phase  $ph$  of this observation can be related to the local longitude  $\varphi$  via

$$ph = 1 - \varphi/(2\pi), \quad (7)$$

and "zero" rotational phase is chosen to be the "Equatorial view ( $0^\circ$ )" as shown in Figure 1.

If selecting a reference epoch, and assuming the rotational phase at this epoch to be  $zph$ , then all the rotational phases of other data could be derived in consideration of the observation time and geometry. Furthermore, for some particular epoch, light curves can be derived for each band by correcting the observed flux at various epochs into one rotation period at this epoch, where the correction is implemented via

$$F_{i,\text{corr}} = F_i \left( \frac{r_{i,\text{helio}}}{r_{0,\text{helio}}} \right)^2 \left( \frac{\Delta_{i,\text{obs}}}{\Delta_{0,\text{obs}}} \right)^2, \quad (8)$$

in which  $F_{i,\text{corr}}$  is the flux after correction,  $F_i$  is the original observed flux,  $r_{i,\text{helio}}$  and  $r_{0,\text{helio}}$  are the heliocentric distance of epoch  $i$  and the reference epoch, while  $\Delta_{i,\text{obs}}$  and  $\Delta_{0,\text{obs}}$  are the observation distance.

Following the above method, firstly we select '2010-01-31 12:06' as the reference epoch for deriving the reference rotational phase  $zph$ . But for correction of flux, in order to reduce flux errors caused by correction Equation (8), we select 28 separate reference epochs, so as to use data close to

each reference epoch (data within three days) to generate infrared light curves. By this way, we obtain 28 infrared light curves. Then for each of the reference epoch, theoretical infrared light curves are simulated by RSTPM to fit the above generated observational light curves. The best-fit results are plotted in Figure 8. Roughly speaking, our modeled infrared light curves match well with all the four-band observational light curves of WISE/NEOWISE in consideration of the observation errors, indicating that our model results are reliable.

To investigate whether Beagle has surface heterogeneity, the ratios of observation/model are plotted as a function of rotation phase for each band respectively in Figure 9, where a clear rotation phase dependent feature is observed in the data of band-W4, W3, and W2, showing that the observation/model ratios appear to be significantly higher around  $ph = 0.2$  and  $0.7$ , whereas the band-W1 data don't show such feature. Since both irregular shape and surface heterogeneity can contribute to the rotational variation of light-curves, and bands of W4, W3, and W2 are thermal emission dominated, so the heterogeneous features of the thermal light curves of WISE/NEOWISE may imply that: 1, the light-curve inversion shape model is not perfect for modeling thermal emission; or 2, the regolith of Beagle may have heterogeneous thermophysical characteristics along longitude.

#### 4. DISCUSSION

The multi-epoch infrared data of WISE/NEOWISE make it possible to probe the regolith characteristics of asteroids in detail. As an example, this work uses 9 years of infrared data from WISE/NEOWISE to study the regolith of Main-Belt Object (656) Beagle by the well-tested thermophysical model — RSTPM (Yu & Ip 2021). Details about the data processing, fitting procedure, modelling and analyzing of infrared light curves are presented. The results show that Main-Belt Object Beagle has a low mean thermal inertia of  $\Gamma = 14 \sim 32 \text{ Jm}^{-2}\text{s}^{-0.5}\text{K}^{-1}$ , being consistent with that of most large main belt objects (MacLennan & Emery 2021, 2022; Huang et al. 2022); and Beagle has a geometric visual albedo as low as  $0.043 \sim 0.054$ , being far lower than the geometric albedos of its neighbouring asteroids (mean  $p_v = 0.0941 \pm 0.0055$ ) (Fornasier et al. 2016), even lower than the geometric albedo of (24) Themis ( $p_v = 0.064^{+0.008}_{-0.011}$ ) (Yu & Ip 2021). Although the low albedo  $\sim 0.05$  of Beagle still lies on the edge of  $1\sigma$  range of the Beagle family and the Themis family, it is a little anomalous that the albedos of Beagle's neighbouring asteroids are more close to Themis, rather than Beagle itself.

In addition, Figure 9 shows that Beagle exhibits significant rotation-phase dependent features at band-W4, W3 and W2, but not at W1-band. According to Figure 3, band-W4, W3 and W2 are thermal emission dominated, whereas W1-band is dominated by NIR reflection. So the result implies that the surface of Beagle doesn't have significant heterogeneous NIR reflectivity. As mentioned before, Fornasier et al. (2016) shows that the neighbouring asteroids of Beagle have diverse NIR spectral types, and Beagle is expected to show

heterogeneous NIR features across its surface if Beagle is the parent of those neighbouring asteroids. However, here our result shows that Beagle has no significant heterogeneous NIR reflectivity, indicating that Beagle may be not the parent of its neighbouring asteroids, or surface heterogeneity of Beagle at NIR are eliminated for some reasons, for example, the utilization of imperfect light-curve inversion shape model, which doesn't remove the degeneracy between regional NIR reflectivity and slope.

On the other hand, for band-W4, W3 and W2, if doing comparisons between Figure 9 and 1, we can find that the higher observation/model ratios appear around  $ph = 0.2$  and  $0.7$ , the phases of which Beagle happens to have the minimum cross-section area, implying that the rotation-phase dependent feature of band-W4, W3 and W2 has a strong relationship with the utilized shape model. Also we have done several tests by adjusting the rotation period within  $7.033 \pm 0.001$  to do the fitting procedure, but the above rotation-phase dependent feature remains unchanged, indicating that the utilized shape rather than rotation period is more likely to be cause of the rotation-phase dependent feature. Hence the light-curve inversion shape model from optical light curves is not perfect for infrared light curves, similar phenomenons have been found by Hanus et al. (2015) and Āurech, et al. (2017). Nevertheless, the possibility of heterogeneous regolith thermophysical characteristics across the surface of Beagle remains positive, because it would be reasonable to expect different physical characteristics (e.g. roughness) between the body part and the smaller head part, as such phenomenons have been observed on other asteroids by in-situ space missions, for example (25143) Itokawa (Abe et al. 2006).

#### 5. CONCLUSION

By analyzing 9-years infrared light curves of Beagle from WISE/NEOWISE, we get the following results:

1). Beagle has an effective diameter  $D_{\text{eff}} = 57.3^{+4.5}_{-2.2} \text{ km}$ , geometric albedo  $p_v = 0.05^{+0.004}_{-0.007}$ , mean roughness  $\theta_{\text{RMS}} = 44 \pm 4^\circ$ , mean grain size  $b = 100^{+350}_{-90} (10 \sim 450) \mu\text{m}$ , mean specific heat capacity  $c_p = 173 \sim 516 \text{ Jkg}^{-1}\text{K}^{-1}$ , thermal conductivity  $\kappa = 0.7 \sim 1.3 \times 10^{-3} \text{ Wm}^{-1}\text{K}^{-1}$  and thermal inertia  $\Gamma = 14 \sim 32 \text{ Jm}^{-2}\text{s}^{-0.5}\text{K}^{-1}$ .

2). We confirm that the Beagle has an anomalous low albedo that the albedos of Beagle's neighbouring asteroids are more close to Themis, rather than Beagle itself. In addition, the W1-band NIR light curves of Beagle don't reveal significant heterogeneous NIR reflectivity across the surface of Beagle. This result does not support Beagle to be the parent of its neighbouring asteroids which have diverse NIR spectral types (Fornasier et al. 2016). A possible explanation to these results is that Beagle may be an interloper or a sister, rather than the parent of its neighbouring asteroids including the first MBC 133P. Considering Beagle's albedo anomaly, we prefer to surmise Beagle to be an interloper to the Themis family, although it still remains possible for Beagle being an anomalous member of the Themis family. So our results may add new clues of Beagle probably having no genetic connec-



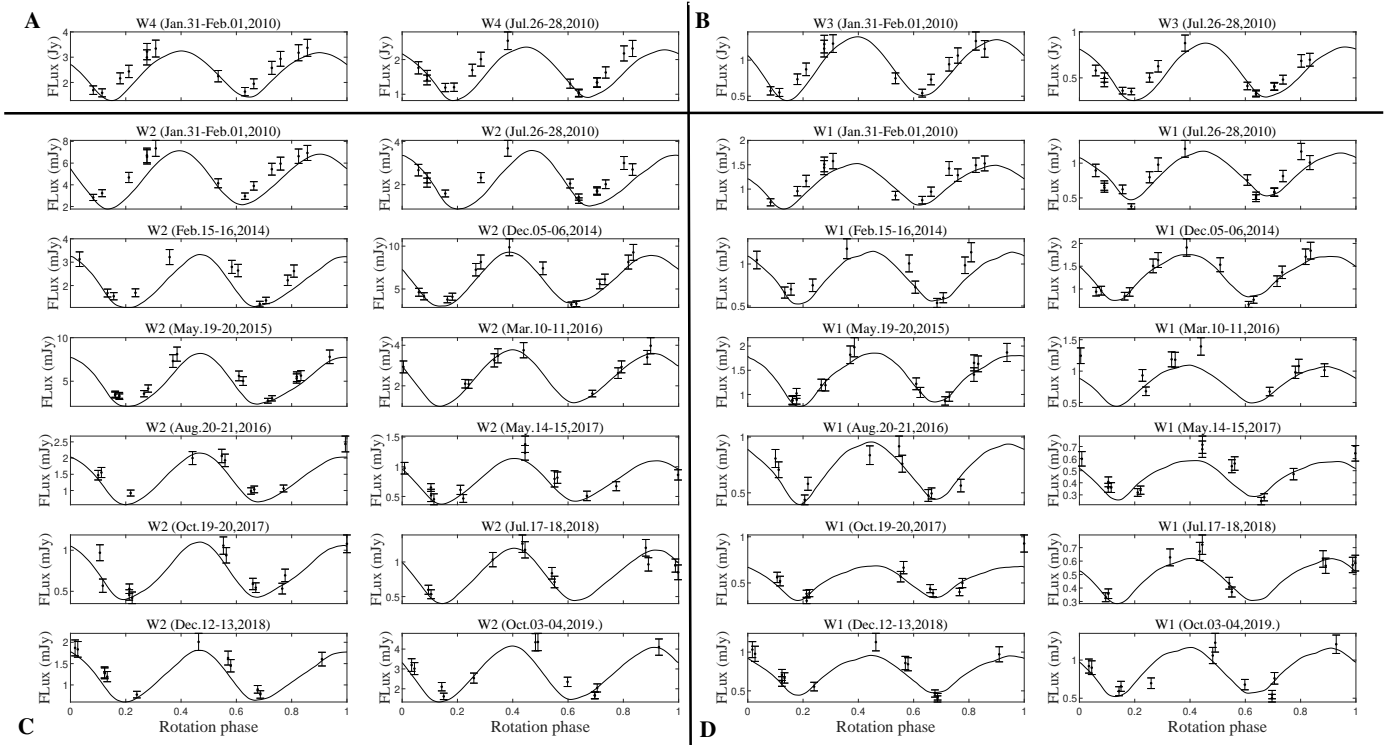


**Figure 8.** Best-fit results to the infrared light curves of WISE/NEOWISE for each observation epoch; Panel A,B,C: thermal light curves at band W4, W3, W2 respectively; Panel D: reflection light curves at band W1.

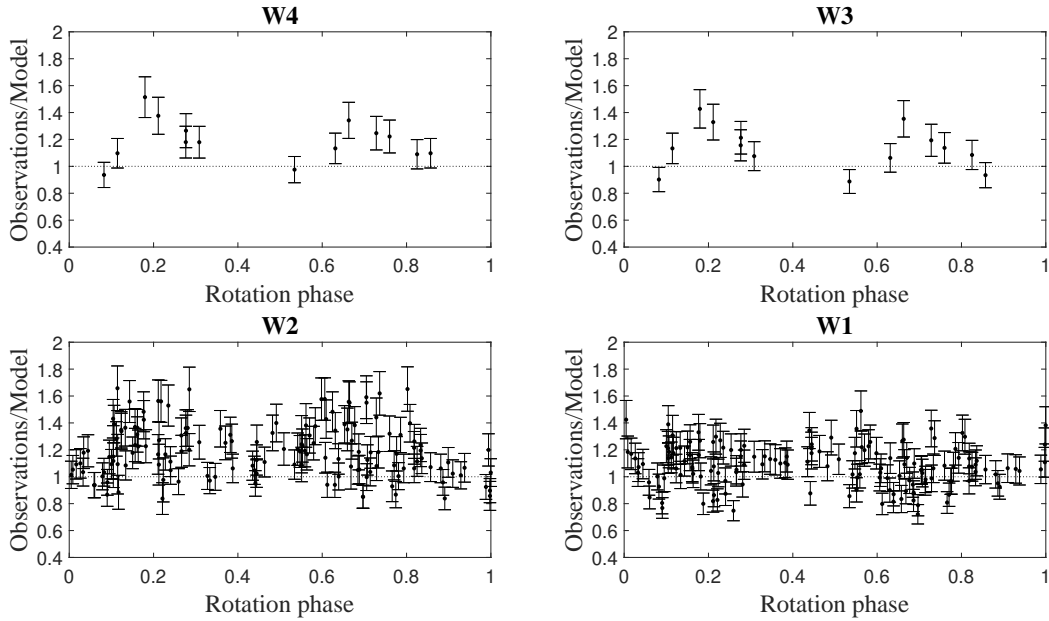


**Figure 9.** Ratios of observation/model as a function of rotation phase for each band respectively.

tion with its neighbouring asteroids and even (24) Themis, and may lead to new scenarios about the origin of the famous MBC 133P.

3). Asteroidal shape models from inversion of optical light curves could have obvious imperfections. As a result, the heterogeneity of surface reflectivity at near infrared is difficult to be discovered if using such shapes to model the theoretical infrared light curves. Besides, the imperfect shapes can also lead to a rotation dependent features in thermal light curves (e.g. band W2, W3, W4 of WISE and NEOWISE), which would mislead the evaluation of the heterogeneity of regolith

thermophysical characteristics. Therefore, to obtain truthful information about the surface heterogeneity of asteroids, it is necessary to input shapes that are more close to reality.

#### ACKNOWLEDGMENTS

We would like to thank the WISE teams for providing public data. This work was supported by the grants from The Science and Technology Development Fund, Macau SAR (File No. 0051/2021/A1). and Faculty Research Grants of The Macau University of Science and Technology (File).

#### REFERENCES

- Abe, M., Takagi, Y., Kitazato, K., Abe, S., et al., 2006. Near-Infrared Spectral Results of Asteroid Itokawa from the Hayabusa Spacecraft, *Science* 312: 1334-1338
- Bowell, E., Hapke, B., Domingue, D., et al., 1989. Application of photometric models to asteroids. In *Asteroids II*, pp. 524-556
- Campins, H., Hargrove, K., Pinilla-Alonso, N., et al., 2010, *Nature*, 464(7293): 1320-1321
- Carruba, V. 2019, *P&SS*, 166, 90
- Cutri, R., Mainzer, A., Conrow, T., et al. 2015, Explanatory Supplement to the NEOWISE Data Release Products, <http://wise2.ipac.caltech.edu/docs/release/neowise/expsup/>
- Cutri, R., Wright, E., Conrow, T., et al. 2012, Explanatory Supplement to the WISE All-Sky Data Release Products, <http://wise2.ipac.caltech.edu/docs/release/allsky/expsup/index.html>
- Ďurech, J., Delbo', M., Carry, B., Hanuš, J., & Alí-Lagoa, V., 2017, *A&A*, 604, A27
- MacLennan, E. M., & Emery, J. P., 2021, *Planet. Sci. J.*, 2(161): 1-12
- MacLennan, E. M., & Emery, J. P., 2022, *Planet. Sci. J.*, 3(47): 1-23
- Fornasier, S., Lantz, C., Perna, D., & Campins, H., et a., 2016, *Icarus*, 269: 1-14
- Hanuš, J., Delbo', M., Ďurech, J., & Alí-Lagoa, V., 2015, *Icarus*, 256, 101
- Huang, D., Hanuš, J., Masiero, J. R., & Tholen, D. J., 2022, *Planet. Sci. J.*, 3(56): 1-25
- Kaasalainen, M., Torppa, J., & Muinonen, K., 2001, 153, 37
- Mainzer, A., Bauer, J., Grav, T., et al. 2011, *ApJ*, 731, 53
- Mainzer, A., Bauer, J., Cutri, R., et al., 2014, *ApJ*, 792, 30
- Mainzer, A. K., Bauer, J. M., Cutri, R. M., et al. 2016, PDSS, EAR-A-COMPIL-5-NEOWISEDIAM-V1.0
- Michel, P., Richardson D. C., Durda D. D., Jutzi M., and Asphaug E., 2015, Collisional formation and modeling of asteroid families. In *Asteroids IV* (P. Michel et al., eds.), pp. 341–354. Univ. of Arizona, Tucson
- Nesvorný, D., Bottke, W. F., Vokrouhlický, D., et al., 2008, *ApJL*, 679: 143-146
- Opeil, C. P., Consolmagno, G. J., Britt, D. T., 2010, *Icarus*, 208, 449-454
- Rivkin, A.S., & Emery, J. P., 2010, *Nature*, 464(7293): 1322-1323
- Rousseau, B., De Sanctis, M. C., Raponi, A., & Ciarniello, M., et al., 2021, *A&A*, 653, 118
- Wright, E. L., Eisenhardt, P. R. M., & Mainzer, A. K., et al., 2010, *AJ*, 140, 1868
- Yu, L. L., Hsia, C.H., & Ip, W. H., 2020, *AJ*, 159(66): 1-10
- Yu L. L., & Ip W. H., 2021, *ApJ*, 913(96): 1-22